

## Article

# NH<sub>2</sub>-Modified UiO-66: Structural Characteristics and Functional Properties

Konstantin L. Timofeev <sup>1</sup>, Sergei A. Kulinich <sup>2,\*</sup>  and Tamara S. Kharlamova <sup>1,\*</sup> <sup>1</sup> Laboratory of Catalytic Research, Tomsk State University, 634050 Tomsk, Russia; kvintkl@gmail.com<sup>2</sup> Research Institute of Science & Technology, Tokai University, Hiratsuka 259-1292, Kanagawa, Japan

\* Correspondence: skulinich@tokai-u.jp (S.A.K.); kharlamova83@gmail.com (T.S.K.)

**Abstract:** The development of new functional materials based on metal–organic frameworks (MOFs) for adsorption and catalytic applications is one of the promising trends of modern materials science. The Zr-based MOFs, specifically UiO-66, are considered as the supports for metallic catalysts for the 5-hydroxymethylfurfural platform molecule reduction into valuable products. The present work focused on the effect of NH<sub>2</sub> modification of UiO-66 on its structure and functional properties. The samples were prepared by a solvothermal method. The structure of the obtained materials was studied by X-ray diffraction, IR spectroscopy, UV–visible spectroscopy, and low-temperature nitrogen adsorption. Basic properties were investigated by HCl and CH<sub>3</sub>COOH adsorption, and electrokinetic properties were studied by electrophoretic light scattering. UiO-66-NH<sub>2</sub> samples with different contents of aminoterephthalate linkers were successfully prepared. A gradual decrease in the specific surface area and the fraction of micropores with a diameter of ~0.9 nm was observed with an increase in the aminoterephthalate content. A proportional increase in the total number of basic sites in UiO-66-NH<sub>2</sub> samples was established with an increase in the aminoterephthalate content up to 75%. At the same time, a noticeable decrease in the total number of basic sites and an increase in their strength with higher aminoterephthalate content was observed.

**Keywords:** UiO-66; UiO-66-NH<sub>2</sub>; structural peculiarities; basic properties; IEP

**Citation:** Timofeev, K.L.; Kulinich, S.A.; Kharlamova, T.S. NH<sub>2</sub>-Modified UiO-66: Structural Characteristics and Functional Properties. *Molecules* **2023**, *28*, 3916. <https://doi.org/10.3390/molecules28093916>

Academic Editors: Rafael Luque, Amarajothi Dhakshinamoorthy and Francisco G. Cirujano

Received: 12 April 2023

Revised: 28 April 2023

Accepted: 4 May 2023

Published: 5 May 2023



**Copyright:** © 2023 by the authors. Licensee MDPI, Basel, Switzerland. This article is an open access article distributed under the terms and conditions of the Creative Commons Attribution (CC BY) license (<https://creativecommons.org/licenses/by/4.0/>).

## 1. Introduction

The use of biomass as an easily renewable source is becoming an increasingly attractive and promising way to obtain a wide range of valuable compounds [1,2]. Among the various biomass-derived products, 5-hydroxymethylfurfural (5-HMF) is considered one of the most promising platform molecules [3–5]. Supported noble metals (Au, Pd, Pt, Ag, etc.) and bimetallic compositions on the basis thereof are the most abundant and well-proven catalytic materials proposed for HMF reduction [4–6]. However, despite the progress made in the development of catalysts for HMF transformation, further catalyst improvement is required, and a support can notably affect the performance.

Recently, metal–organic frameworks (MOFs) have attracted increasing attention in various fields due to their high porosity and variety of structures [7]. Zirconium terephthalate UiO-66 deserves special interest due to its unprecedented stability [8,9]. Modification of UiO-66 by introducing various functional groups and/or metal centers into its structure creates additional functionality of the resulting new materials. The modification of MOFs with NH<sub>2</sub> groups makes it possible to change its acid–base and optical properties as well as to create additional functionality for stabilization of metal particles or further modification [10–14]. Specifically, the Pd/MIL-101(Al)-NH<sub>2</sub> catalyst for the selective 5-HMF hydrogenation to 2,5-dihydroxymethyl-tetrahydrofuran (DHMTFH) was prepared using a direct anionic exchange approach and subsequent soft reduction [10], with the presence of free amine moieties being suggested to play the key roles in the formation of uniform and well-dispersed palladium nanoparticles on the support. Moreover, the observed high

selectivity towards DHMTHF was closely related to the cooperation between the metallic site and the free amine moiety on the MOF support in the Pd/MIL-101(Al)-NH<sub>2</sub> catalyst.

A similar approach was used to prepare the Pd@NH<sub>2</sub>-UiO-66 catalyst for the vanillin hydrodeoxygenation in water [11]. A photoinduction method including Cu species adsorption by NH<sub>2</sub> groups of the UiO-66-NH<sub>2</sub> support followed by their anchoring after irradiation with visible light was successfully used to construct single-atom Cu/UiO-66-NH<sub>2</sub> as a robust photocatalyst for CO<sub>2</sub> conversion to liquid fuels [15]. In this case, Cu species anchored were optimized the structure of photocatalysts at the atomic level to facilitate the separation of electron–hole pairs. The Cu(II)@UiO-66-NH<sub>2</sub> and Cu(0)@UiO-66-NH<sub>2</sub> catalytic materials were generated via the simple impregnation of nano-sized UiO-66-NH<sub>2</sub> with Cu(OAc)<sub>2</sub> solution and the subsequent metal ion reduction process, respectively [16]. Spherical-shaped copper particles uniformly distributed in Cu(0)@UiO-66-NH<sub>2</sub> material with an average size of 4–6 nm were revealed by HRTEM, indicating the formation of Cu NPs primarily on the external surface than in the pores of the MOFs characterized by the structure with cavities of ~9 and ~11 Å. Highly dispersed Au nanoparticles were immobilized on amino-functionalized UiO-66-NH<sub>2</sub> MOFs via the absorption/reduction method in solution [17], with the amino functionality of the MOF being considered to rapidly coordinate with HAuCl<sub>4</sub> and act as the Au(0) precursor. However, the primary formation of Au NPs coated on the external surface of the MOFs was reported for Au@UiO-66-NH<sub>2</sub> composites prepared using similar approaches [18,19].

The formation of bimetallic composites based on UiO-66-NH<sub>2</sub> was also described. Thus, Au–Pd@UiO-66-NH<sub>2</sub> heterogeneous catalysts for reductive amination of benzaldehyde with extremely low Pd loading and Au/Pd@UiO-66-NH<sub>2</sub> (Au:Pd = 1:1, 1:2, 2:1) photocatalysts for the liquid-phase Suzuki–Miyaura coupling reaction were prepared by a one-pot absorption–reduction method [20,21]. However, the confirmation of the formation of alloyed particles in both cases was rather speculative. The formation of Au particles was revealed by XRD and UV–vis spectroscopy data for Au/Pd@UiO-66-NH<sub>2</sub> photocatalysts [21].

Therefore, the results reported for metal-loaded metal–organic frameworks, specifically metal@NH<sub>2</sub>-UiO-66 materials, strongly differ even for similar preparation approaches, with the size, composition, and location of metal particles strongly affecting the material performance [22,23]. This indicates that such strategies are still developed by trial and error to some extent, and an in-depth understanding of the mechanism of formation is still lacking, especially for bimetallic systems. Specifically, the Zr<sub>6</sub>O<sub>4</sub>(OH)<sub>4</sub> clusters can also play the key role in the metal particle formation in UiO-66-NH<sub>2</sub>-based materials along with the amino group. Further, to create the bifunctional systems with redox and acid–base species, it is important to study acid–base properties of the materials under conditions close to those of the reaction medium. Thus, more extensive studies of the structure peculiarities and functional properties of the NH<sub>2</sub>-modified UiO-66 MOFs are highly desired for purposeful design of the UiO-66-based bimetallic catalysts.

The present work is focused on the study of crystal and pore structure peculiarities and functional properties of NH<sub>2</sub>-modified UiO-66 considered as a support for PdCu and PdAu catalysts for 5-HMF reduction in water solutions.

## 2. Results and Discussion

UiO-66 and UiO-66-NH<sub>2</sub>-X (where X is a fraction of aminoterephthalate linkers) samples with different contents of aminoterephthalate linkers were prepared by a solvothermal method. The morphologies of UiO-66 and UiO-66-NH<sub>2</sub>-X crystals were characterized by scanning electron microscopy (SEM). The structure of the obtained materials was studied by X-ray diffraction (XRD), IR spectroscopy, UV–vis spectroscopy, and low-temperature N<sub>2</sub> adsorption. Basic properties were investigated by HCl and CH<sub>3</sub>COOH adsorption from water solutions, and electrokinetic properties were studied by electrophoretic light scattering.

## 2.1. Structural Characteristics

### 2.1.1. SEM and X-ray Diffraction

The samples prepared were formed by small (<300 nm) crystals (Figure S1). The UiO-66 crystal structure was confirmed by XRD for all samples obtained. The XRD patterns of the samples (Figure 1) contain characteristic reflections of the cubic UiO-66 (ICDD PDF-4 card #71-0285), and Table 1 represents a lattice parameter,  $a$ , and a unit cell volume,  $V$ . According to the results obtained, the increase in the aminoterephthalate content in the UiO-66 structure is accompanied by some lattice compression. Specifically, the unit cell volume gradually decreases from 9077 Å<sup>3</sup> for the UiO-66 sample to 8960 Å<sup>3</sup> for the UiO-66-NH<sub>2</sub>-75 sample as the aminoterephthalate content is increased. A slight increase in the unit cell in volume is observed for the UiO-66-NH<sub>2</sub>-100 sample as compared with the UiO-66-NH<sub>2</sub>-75 sample but it remains lower than that for other samples. These results are consistent with those presented in [24–26], where the XRD reflection shift to higher values is observed for UiO-66-NH<sub>2</sub> MOFs.

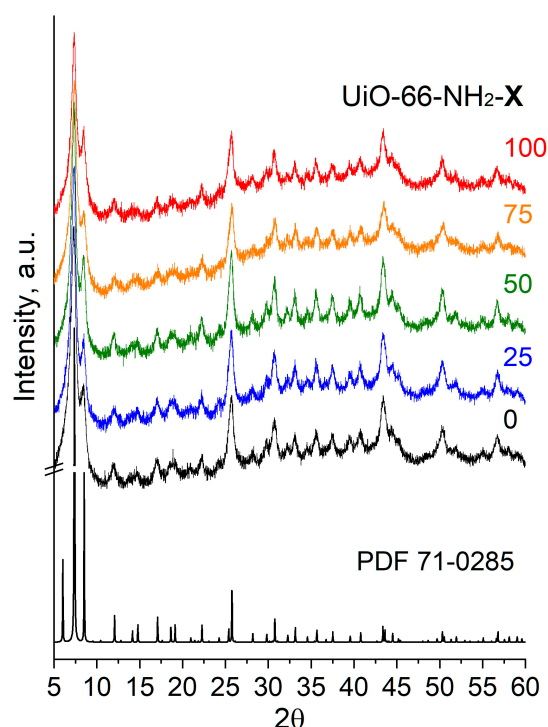


**Figure 1.** XRD patterns for UiO-66 ( $X = 0$ ) and UiO-66-NH<sub>2</sub>- $X$  samples.

**Table 1.** XRD (lattice parameter  $a$ ; unit cell volume  $V$ ) and low-temperature adsorption data (specific surface area (SSA); specific volume of micropore ( $V_{HK}$ ) and mesopore ( $V_{BJH}$ )).

Sample	SG	$a$ , Å	$V$ , Å <sup>3</sup>	SSA, m <sup>2</sup> /g	$V_{HK}$ , cm <sup>3</sup> /g	$V_{BJH}$ , cm <sup>3</sup> /g
UiO-66	Pm-3m	20.86	9077	1269	0.50	0.83
UiO-66-NH <sub>2</sub> -25	Pm-3m	20.83	9037	1091	0.43	0.40
UiO-66-NH <sub>2</sub> -50	Pm-3m	20.83	9037	1158	0.45	0.31
UiO-66-NH <sub>2</sub> -75	Pm-3m	20.77	8960	825	0.33	0.28
UiO-66-NH <sub>2</sub> -100	Pm-3m	20.80	8999	854	0.34	0.24

### 2.1.2. IR Spectroscopy

To confirm the formation of NH<sub>2</sub>-modified UiO-66 and study its structural peculiarities, the samples were studied by IR spectroscopy. Figure 2 shows the IR spectra for the samples containing a number of characteristic bands within the range from 500 to 1900 cm<sup>-1</sup>. Figure S2 shows the expanded views of subregion 2600–3200 cm<sup>-1</sup> (Supplementary Materials).

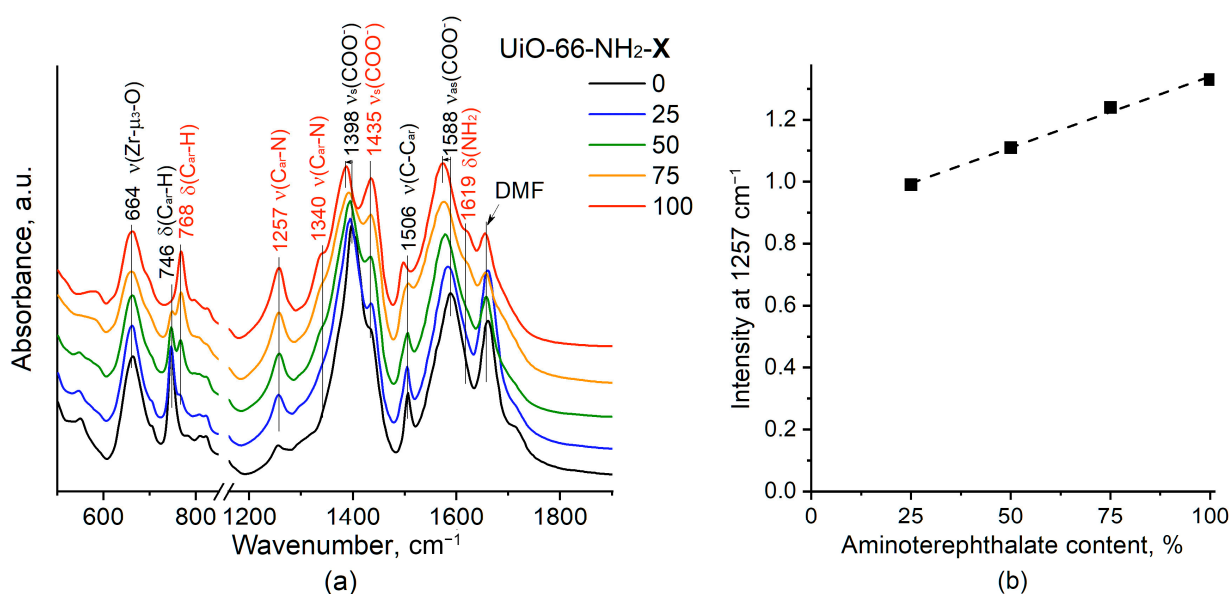


**Figure 2.** IR spectra for UiO-66 (X = 0) and UiO-66-NH<sub>2</sub>-X samples (a) and dependence of ν(C<sub>ar</sub>-N) band intensity on the aminoterephthalate content in the sample (b). DMF is dimethylformamide.

The spectrum for the pristine UiO-66 contains the bands at 1397 and 1589 cm<sup>-1</sup> assigned to COO<sup>-</sup> stretching vibrations, at 1506 and 746 cm<sup>-1</sup> associated with C-C and C-H vibrations in the benzene ring, respectively, and at 664 cm<sup>-1</sup> attributed to μ<sub>3</sub>-O stretching in Zr<sub>6</sub>O<sub>4</sub>(OH)<sub>4</sub> clusters [27,28]. A band at 1660 cm<sup>-1</sup> is due to the dimethylformamide (DMF) residual [29].

For the UiO-66-NH<sub>2</sub> samples, new bands at 1257 and 1340 cm<sup>-1</sup> assigned to C-N stretching vibrations as well as at 1619, 3367, and 3453 cm<sup>-1</sup> assigned to NH<sub>2</sub> group vibrations appear (see subregion 2600–3200 cm<sup>-1</sup> in Figure S2) [27]. Further, the appearance of a new band at 768 cm<sup>-1</sup> assigned to C-H vibrations in the NH<sub>2</sub>-substituted benzene ring as well as a gradual shift in COO<sup>-</sup> stretching vibration bands to lower wavenumbers accompanied by a splitting of symmetric COO<sup>-</sup> stretching vibrations (decrease in the intensity of the band at 1387–1398 cm<sup>-1</sup> and appearance of a new band at 1435 cm<sup>-1</sup>) is observed due to the NH<sub>2</sub> group effect. The intensity of the nonoverlapping band at 1257 cm<sup>-1</sup> proportionally increases with the increase in the aminoterephthalate content in the sample, indicating the formation of UiO-66-NH<sub>2</sub> MOFs with different amounts of NH<sub>2</sub> groups (Figure 2b).

### 2.1.3. UV-Vis Spectroscopy

The optical properties of the samples were studied by UV-vis spectroscopy. Figure 3 shows UV-vis spectra for UiO-66 and UiO-66-NH<sub>2</sub>-X samples. The spectrum for the former is characterized by the absorption below 320 nm caused by π-π\* electronic transition of the biphenyl linker system [24,30]. In spectra for the UiO-66-NH<sub>2</sub>-X sample, an absorption band with a maximum at 364 nm caused by the electronic transition from the nonbonding to antibonding molecular orbital of aminoterephthalate (n → π\*) is additionally present [24,30,31]. The intensity of this band increases with an increase in the aminoterephthalate content according to the Beer-Lambert law (Figure 3b), which is consistent with the IR spectroscopy data, indicating the formation of UiO-66-NH<sub>2</sub> MOFs with different numbers of NH<sub>2</sub> groups.

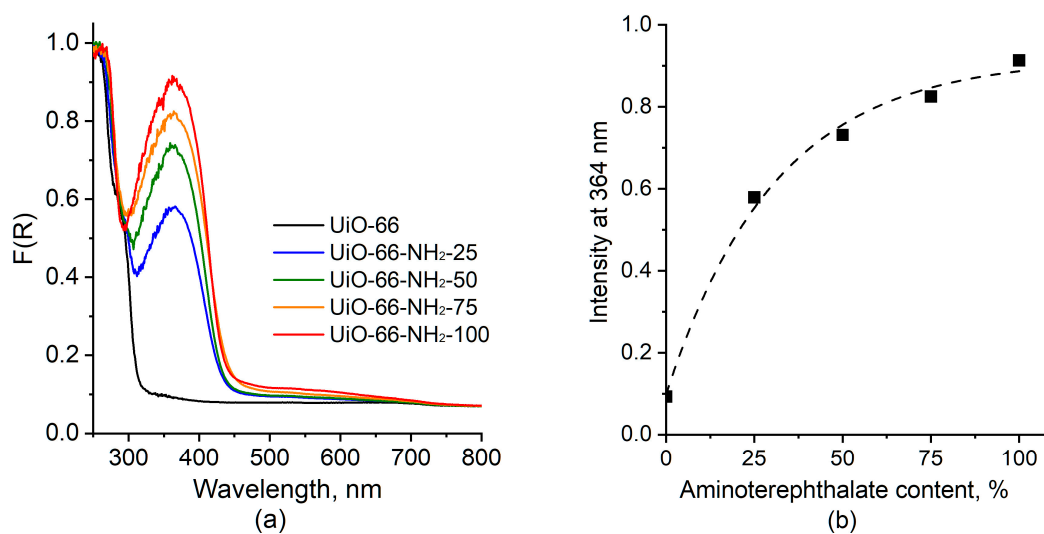


**Figure 3.** UV-vis spectra for UiO-66 ( $X = 0$ ) and UiO-66-NH<sub>2</sub>- $X$  samples (a) and dependence of the intensity at 364 nm on the aminoterephthalate content in the sample (b).

#### 2.1.4. Textural Characteristics

Figure 4 shows the isotherms of low-temperature N<sub>2</sub> adsorption–desorption for UiO-66 and UiO-66-NH<sub>2</sub>- $X$  samples, and Table 1 shows the values of specific surface area (SSA) and pore volumes of micropores ( $V_{HK}$ ) and mesopores ( $V_{BJH}$ ).

According to the IUPAC classification [32], all samples are characterized by type I isotherms typical for microporous materials with a hysteresis loop of the H4 type (Figure 4a). The steep uptake at rather low relative pressures ( $<0.05$ ) is due to the micropore filling caused by the enhanced adsorbent–adsorptive interactions in narrow micropores. The presence of the hysteresis loop in the range of 0.8–1.0  $p/p_0$  indicates that the sample contains mesopores due to the defects in the UiO-66 structure and gaps between the particles in aggregates. In general, a gradual decrease in the specific surface area and pore volume of the samples is observed with an increase in the aminoterephthalate content in the sample (Table 1). The deviations from the monotonic decrease in the SSA and pore volume do not exceed a 10% error when they are determined from the low-temperature nitrogen adsorption data. The observed decrease in SSA and pore volume are attributed to both reduced available free space and increased overall weight of the UiO-66-NH<sub>2</sub>- $X$  samples.

The unmodified UiO-66 sample is characterized by a bimodal distribution of micropores with maxima at  $\sim 0.9$  nm and  $\sim 0.6$  nm (Figure 4c) that is typical for the UiO-66 [33–35]. The observed bimodal distribution is consistent with a change in the size of the pore entrance formed by the terephthalate bridges between the Zr<sub>6</sub>O<sub>4</sub>(OH)<sub>4</sub> sites as a result of a change in the orientation of benzene rings due to the flips around the C<sub>2</sub> symmetry axis [36]. Specifically, the benzene rings were shown to flip, changing the pore entrance size to 3.7, 6, and 9.2 Å (Figure 4d), with latter two sizes being available for determination by the low-temperature N<sub>2</sub> adsorption and the smaller pores being outside the detection range of the method.

For the UiO-66-NH<sub>2</sub>- $X$  samples, a gradual decrease in the volume for pores with a diameter of  $\sim 0.9$  nm is observed in the micropore size distribution as the aminoterephthalate content increases (Figure 4c). For the UiO-66-NH<sub>2</sub>-100 sample, only micropores with a diameter of  $\sim 0.6$  nm is present. The observed change in the pore size distribution was associated with the hindered flips of the NH<sub>2</sub>-substituted benzene rings around the C<sub>2</sub> symmetry axis and the predominant orientation of benzene rings corresponding to micropore sizes of  $\sim 0.6$  nm in the detection range of the low-temperature N<sub>2</sub> adsorption at least at  $-195.8$  °C. This does not exclude orientation of benzene rings corresponding to micropore sizes with the smaller entrance radius (outside the detection range) as well

as the possibility of rotation of the  $\text{NH}_2$ -substituted benzene ring at higher temperatures. The effect of  $\text{NH}_2$  groups, which are larger than H atoms, on micropore size distribution for UiO-66- $\text{NH}_2$ -X samples also cannot be ruled out [37].

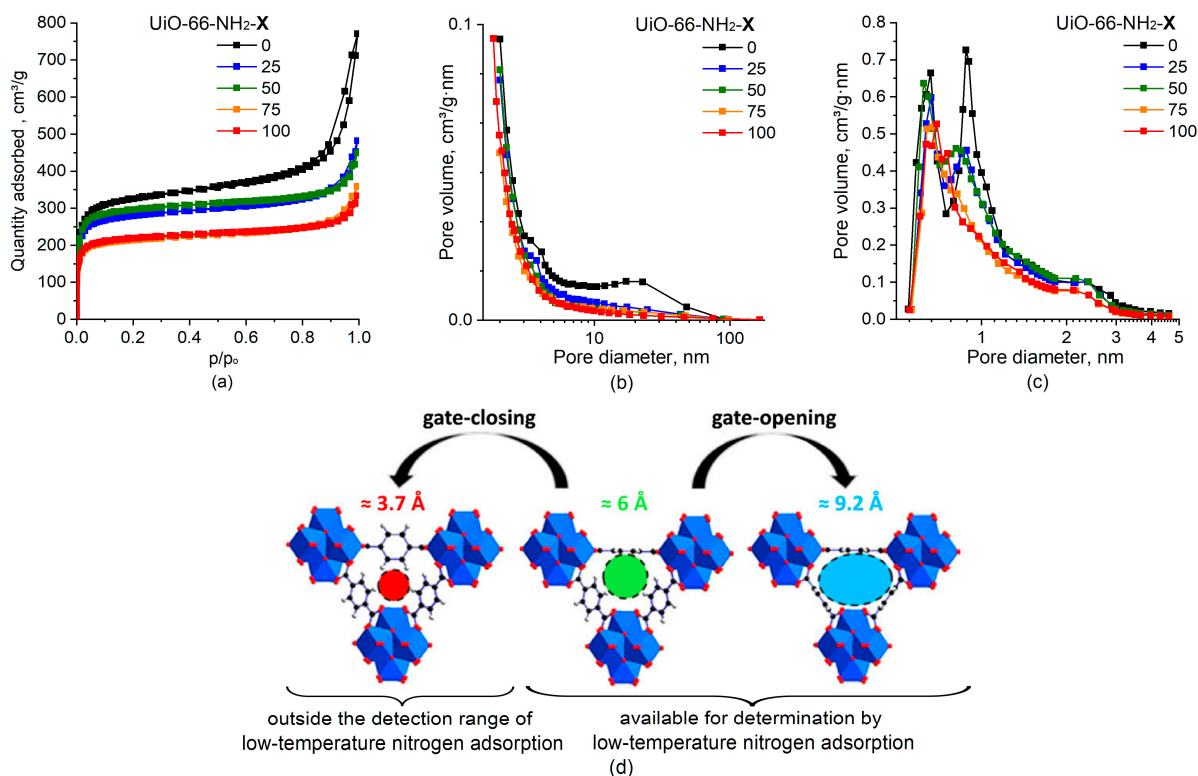


**Figure 4.** Adsorption isotherms (a) and mesopore size distribution according to the BJH desorption method (b) and micropore size distribution according to the Horvath–Kawazoe method (c) for UiO-66 ( $X = 0$ ) and UiO-66- $\text{NH}_2$ -X samples. Change in pore entrance size as a result of the three oriented benzene rings flipping around the  $\text{C}_2$  symmetry axis (d). Adapted with permission from [36]; copyright 2017 American Chemical Society.

## 2.2. Functional Properties

### 2.2.1. Electrokinetic Properties

The water dispersions of UiO-66 and UiO-66- $\text{NH}_2$ -X samples were characterized by an initial pH of  $\sim 3.7$  and a zeta potential of  $30.7 \pm 1.2$  mV independent of their composition. The pH increase resulted in rapid decrease in the surface charge (Figure S3, exemplified by the UiO-66 and UiO-66- $\text{NH}_2$ -75 samples), with the IEP being at a pH of 4.4–4.7. Similar results were reported for UiO-66- $\text{NH}_2$  [38]. Comparable zeta potential dependences for UiO-66 and UiO-66- $\text{NH}_2$  MOFs (but characterized by the IEP at a pH of 5.6) were observed in [39]. The observed difference in the IEP can be caused by differences in experimental conditions, including temperature, the error in pH measurements, and the presence of impurities [40].

Independence of electrokinetic properties of the samples on their composition indicates that those are primarily related to  $\text{Zr}_6\text{O}_4(\text{OH})_4$  clusters due to the formation of surface  $-\text{ZrOH}_2^+$ ,  $-\text{ZrOH}$  and  $-\text{ZrO}^-$  groups in water at different pH but not to linkers.

### 2.2.2. Basic Properties

The basic properties of the UiO-66 and UiO-66- $\text{NH}_2$ -X samples were studied by the adsorption of acids from aqueous solutions. HCl and  $\text{CH}_3\text{COOH}$  were used as strong and weak acid to determine the total number of basic sites and strong basic sites, respectively. Figure 5a shows the results obtained. The pristine UiO-66 is characterized by the relatively

low (0.9 mmol/g) number of basic sites predominantly characterized by strong basicity. These basic sites are assigned to the basicity of  $Zr_6O_4(OH)_4$  clusters (Figure 5b) [41–43].

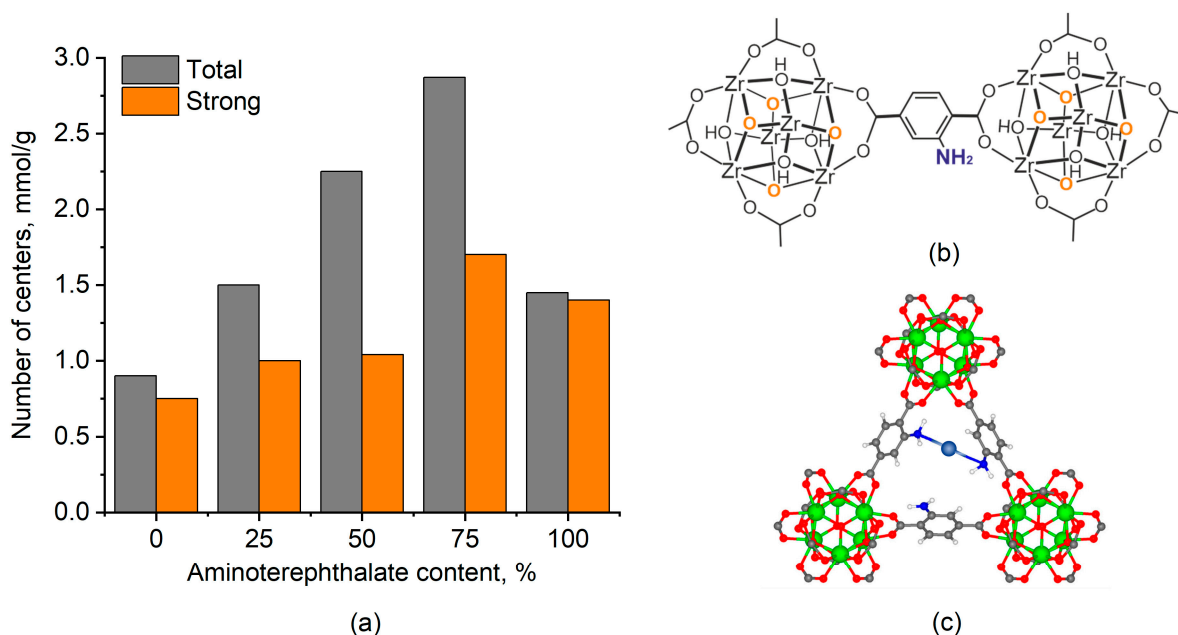


**Figure 5.** Dependence of the number of basic sites on the aminoterephthalate content in UiO-66 ( $X = 0$ ) and UiO-66-NH<sub>2</sub>-X samples (a). Illustrative depiction of basic sites in UiO-66-NH<sub>2</sub>-X samples: basic sites in  $Zr_6O_4(OH)_4$  clusters indicated by orange and NH<sub>2</sub> group of aminoterephthalate linker indicated by blue (b). The local atomic structure model of multicordinated atoms exemplified by isolated Cu species coordinated to two N atoms on UiO-66-NH<sub>2</sub> according to [15] (c). Adapted with permission from [15]; copyright 2020 American Chemical Society.

A gradual increase in the total number of basic sites up to 2.75 mmol/g with the increase in the aminoterephthalate content in the UiO-66-NH<sub>2</sub>-X samples up to 75% is observed but the complete replacement of terephthalate in the UiO-66-NH<sub>2</sub>-100 sample with aminoterephthalate is accompanied by a sharp decrease in the total number of basic sites up to 1.5 mmol/g. The number of strong basic sites increases insignificantly up to the aminoterephthalate content in UiO-66-NH<sub>2</sub>-X sample of 50%, which is consistent with low basicity of aryl amines due to the nitrogen electron pair delocalization [44]. However, at the higher aminoterephthalate content, the number of strong basic sites notably increases, and almost all sites in the UiO-66-NH<sub>2</sub>-100 sample are strong. The observed decrease in the total number of basic sites accompanied by the increase in the strong site fraction was associated with the formation of sites related to a proton multicordinated between several nitrogen atoms [45]. The formation of multicordinated species in MOFs was recently revealed for isolated Cu species anchored on UiO-66-NH<sub>2</sub> by element-selective X-ray absorption fine structure measurements [15]. Specifically, the results obtained illustrated that the isolated Cu atoms were coordinated to two N atoms with atom distances of 1.97 Å (Cu–N). The local atomic structure model of such Cu species is shown in Figure 5c. In case of the proton, the sharp decrease in the total number of basic sites indicates that it requires to be coordinated to more N atoms to form multicordinated species.

### 2.3. UiO-66-NH<sub>2</sub> as a Support

The UiO-66-NH<sub>2</sub> MOFs attracts attention as a support for the fabrication of metal@MOF hybrid catalysts because of its high thermal and chemical stability, large accessible pore volume, and the amine groups within UiO-66-NH<sub>2</sub> serving as the coordination sites for metal ions. The IR and UV–vis spectroscopy data indicate that the amount of NH<sub>2</sub> moieties can be easily controlled by varying the ratio of terephthalic and aminoterephthalic acids

during MOF synthesis by the solvothermal method. This provides additional opportunities to control the distribution and size of metal particles formed with the participation of  $\text{NH}_2$  groups.

Various mechanisms for the metal precursor anchoring with the participation of  $\text{NH}_2$  groups are described in the literature, including electrostatic interaction between the  $-\text{NH}_3^+$  cation formed via amino group protonation and the anion ( $-\text{NH}_3^+ \{\text{PdCl}_4\}^{2-}$ ) [10,21], the coordination interaction between the  $\text{NH}_2$  group and the metal cation by a lone pair of electrons on nitrogen [46], etc. At the same time, according to the studies of basic properties of  $\text{UiO-66-NH}_2\text{-X}$ , the amino groups in the  $\text{UiO-66-NH}_2\text{-X}$  exhibit weak basic or electron-donating properties, which limits the adsorption of precursors with their participation. The electron-accepting ability of the metal ions, and, as a result, their adsorption, can be controlled by pH, temperature, and concentrations of initial ions [46]. Further, the fraction of amino groups in  $\text{UiO-66-NH}_2\text{-X}$  MOFs can also affect the sorption capacity and adsorption strength due to multicenter adsorption as it was revealed for proton adsorption in this study and for Cu single atoms in  $\text{UiO-66-NH}_2$  [15]. This understanding is consistent with the formation of Cu NPs for  $\text{Cu(0)@UiO-66-NH}_2$  with a Cu content of 3.5 wt% [16] and Cu single atoms for  $\text{Cu SAs@UiO-66-NH}_2$  with a Cu content of 0.3 wt% [15]. In the case of bimetallic systems, it is also necessary to consider the possible competitive sorption of precursor ions.

The results of the electrokinetic studies indicate that  $\text{Zr}_6\text{O}_4(\text{OH})_4$  clusters in the  $\text{UiO-66-NH}_2\text{-X}$  materials can also play an important role in the interaction with the precursors of deposited metals. Specifically, at low pH, the  $\text{UiO-66-NH}_2\text{-X}$  samples are characterized by a high positive charge due to the formation of surface  $-\text{ZrOH}_2^+$  species, which should promote the adsorption of  $\text{AuCl}_4^-$  and  $\text{PdCl}_4^{2-}$  anions.

Therefore, the results obtained for the  $\text{UiO-66-NH}_2\text{-X}$  provide insight for the purposeful design of metal@MOF hybrid catalysts.

### 3. Materials and Methods

#### 3.1. Materials Preparation

$\text{UiO-66}$  and  $\text{UiO-66-NH}_2$  samples ( $\text{UiO-66-NH}_2\text{-X}$ , where X is a fraction of aminoterephthalate linkers) were prepared by a solvothermal method using  $\text{ZrO}(\text{NO}_3)_2 \times \text{H}_2\text{O}$  as a precursor of Zr and terephthalic acid and/or 2-aminoterephthalic acid as linkers, HCl as a modulator, and DMF as a solvent.  $\text{ZrO}(\text{NO}_3)_2 \times \text{H}_2\text{O}$  was dissolved in DMF with HCl at  $120^\circ\text{C}$ . Terephthalic acid and/or 2-aminoterephthalic acid was dissolved in DMF at  $120^\circ\text{C}$  in a round-bottomed flask. Then, the  $\text{ZrO}(\text{NO}_3)_2$  solution was added to the acid solution and heated at  $120^\circ\text{C}$  and vigorous stirring for 1 h in a closed flask for hydrothermal reaction. After cooling, the resulting solid was filtered, immersed twice in DMF for 12 h followed by filtration to remove unreacted terephthalic acid. Then, it was immersed in ethanol for 12 h, and in acetone for 12 h to remove DMF, and dried at room temperature.

#### 3.2. Low-Temperature Nitrogen Adsorption

Low-temperature nitrogen adsorption at  $-196^\circ\text{C}$  was carried out using the 3Flex (Micromeritics, Norcross, GA, USA) gas-adsorption analyzer of specific surface area and porosity. Prior to the experiments, the samples were degassed at  $200^\circ\text{C}$  under vacuum ( $10^{-2}$  Torr) for 2 h using the VacPrep Degasser (Micromeritics, Norcross, GA, USA). The specific surface area was determined by the Brunauer–Emmett–Teller (BET) method. The mesopore size distribution was determined by the Barrett–Joyner–Halenda (BJH) desorption method, and the micropores size distribution was determined by the Hovarth–Kowazoe method.

#### 3.3. X-ray Diffraction

XRD patterns of the samples were obtained on the X-ray diffractometer XRD-7000 (Shimadzu, Japan) with a monochromatic  $\text{CuK}\alpha$  radiation ( $1.54 \text{ \AA}$ ) in the  $2\theta$  range of  $5\text{--}60^\circ$  and a scanning rate of  $0.02^\circ/\text{s}$ . The data were obtained using the Bragg–Brentano geometry. Crystalline Si ( $a = 5.4309 \text{ \AA}$ ,  $\lambda = 1.540562 \text{ \AA}$ ) was used as an external standard for



diffractometer calibration. The phase composition of the samples was analyzed using the PDF-4 database (Release 2021 RDB).

### 3.4. IR Spectroscopy

IR spectra were obtained on the Tensor 27 IR-Fourier spectrometer (Bruker, Germany) in the transmission mode using the KBr pressing method in the range of 350–4000  $\text{cm}^{-1}$  with a resolution of 4  $\text{cm}^{-1}$ .

### 3.5. UV–Vis Spectroscopy

Absorption spectra in the UV–visible region were recorded on the Cary100 spectrophotometer (Varian, Mulgrave, VIC, Australia) in a diffuse reflection (DR) mode using the DRA-CA-30I accessory (Labsphere, USA) in the wavelength range of 300–800 nm with a step of 1 nm using the quartz cuvette with an optical path length of 2 mm. MgO was used as a reference sample. The samples were mixed with MgO prior to study in a mass ratio sample/MgO = 1/9. The reflection spectra were transformed into the absorption spectra using the Kubelka–Munk function:

$$F(R) = (1 - R)^2 / (2R),$$

where R is the reflection factor.

### 3.6. Electrophoretic Light Scattering

The electrokinetic properties of the dispersions were studied by electrophoretic light scattering (ELS) using the phase analysis light scattering (PALS) technique on the Omni S/N analyzer (Brookhaven, NY, USA) equipped with the BI-ZTU autotitrator (Brookhaven, NY, USA). For study, the samples were dispersed in a distilled water at a concentration of 25 mg/L using ultrasound for 3 min. To determine the pH of the isoelectric point (IEP), the dispersion was titrated using the diluted (0.001 and 0.1 mol/L) KOH solutions.

### 3.7. Acid Adsorption

The basic properties of the samples were studied by the adsorption of acids from aqueous solutions [47,48]. HCl was used to determine the total number of basic sites, while  $\text{CH}_3\text{COOH}$  was used to determine the strong basic sites. For the study, 0.5 g of the sample was suspended in 50 mL of an aqueous solution of HCl or  $\text{CH}_3\text{COOH}$  (0.1 mol/L). The suspension was thoroughly stirred for 1 h at room temperature. Then, the suspension was filtered, and the filtrate was titrated potentiometrically with an aqueous KOH solution (0.1 mol/L). The titration potential was measured with the pH meter/ionometer ITAN (LLC SPE Tomanalit, Tomsk, Russia). The basicity was calculated as follows:

$$N = \frac{(C_0 - C_1)V_0}{m}$$

where  $N$  is the concentration of basic sites, mol/g;  $C_0$  is the concentration of the acid solution before adsorption, mol/L;  $V_0$  is a volume of the acid solution used, L;  $C_1$  is the concentration of the acid solution after adsorption, mol/L;  $m$  is a weight of the sample.

### 3.8. Scanning Electron Microscopy

The morphology of the materials was studied using a Vega 3 SBH scanning electron microscope (SEM) (Tescan, Brno, Czech Republic).

## 4. Conclusions

A series of  $\text{NH}_2$ -modified UiO-66 samples with different contents of aminoterephthalate linkers was studied. The amount of  $\text{NH}_2$  moieties in UiO-66- $\text{NH}_2$  can be easily controlled by varying the ratio of terephthalic and aminoterephthalic acids during MOF synthesis. The UiO-66 crystal structure was confirmed by XRD for all materials obtained,

with the increasing fraction of aminoterephthalate in the UiO-66-NH<sub>2</sub> framework being confirmed by the IR and UV–vis spectroscopies. The UiO-66 modification with NH<sub>2</sub> groups accompanied by changes in pore structure, optical and basic/electron-donating properties of the materials can affect the characteristics of the catalyst on the basis thereof.

**Supplementary Materials:** The following supporting information can be downloaded at: <https://www.mdpi.com/article/10.3390/molecules28093916/s1>, Figure S1: Typical SEM images of UiO-66 and UiO-66-NH<sub>2</sub>-75 samples. Figure S2: IR spectra for UiO-66 (X = 0) and UiO-66-NH<sub>2</sub>-X samples in subregion 2600–3200 cm<sup>-1</sup>. Figure S3: Zeta potential dependences for UiO-66 and UiO-66-NH<sub>2</sub>-75 samples on pH.

**Author Contributions:** Conceptualization, T.S.K.; methodology, T.S.K.; formal analysis, T.S.K. and K.L.T.; investigation, K.L.T.; writing—original draft preparation, T.S.K. and K.L.T.; writing—review and editing, T.S.K. and S.A.K.; visualization, T.S.K.; supervision, S.A.K.; project administration, T.S.K.; funding acquisition, T.S.K. All authors have read and agreed to the published version of the manuscript.

**Funding:** This research was financially supported by the Russian Science Foundation, grant no. 23-23-00173, <https://rscf.ru/en/project/23-23-00173/> (accessed on 11 April 2023).

**Data Availability Statement:** Not applicable.

**Acknowledgments:** The authors acknowledge A.G. Golubovskaya (Tomsk State University) for SEM study, and M.A. Salaev (Tomsk State University) for language review.

**Conflicts of Interest:** The authors declare no conflict of interest.

## References

1. Chandel, A.K.; Garlapati, V.K.; Jeevan Kumar, S.P.; Hans, M.; Singh, A.K.; Kumar, S. The role of renewable chemicals and biofuels in building a bioeconomy. *Biofuels Bioprod. Biorefining* **2020**, *14*, 830–844. [[CrossRef](#)]
2. Velvizhi, G.; Balakumar, K.; Shetti, N.P.; Ahmad, E.; Pant, K.K.; Aminabhavi, T.M. Integrated biorefinery processes for conversion of lignocellulosic biomass to value added materials: Paving a path towards circular economy. *Bioresour. Technol.* **2022**, *343*, 126151. [[CrossRef](#)] [[PubMed](#)]
3. Timofeev, K.L.; Vodyankina, O. Selective oxidation of bio-based platform molecules and their conversion products over metal nanoparticle catalysts: A review. *React. Chem. Eng.* **2021**, *6*, 418–440. [[CrossRef](#)]
4. Hu, L.; Lin, L.; Wu, Z.; Zhou, S.; Liu, S. Recent advances in catalytic transformation of biomass-derived 5-hydroxymethylfurfural into the innovative fuels and chemicals. *Renew. Sustain. Energy Rev.* **2017**, *74*, 230–257. [[CrossRef](#)]
5. Xu, C.; Paone, E.; Rodriguez-Padron, D.; Luque, R.; Mauriello, F. Recent catalytic routes for the preparation and the upgrading of biomass derived furfural and 5-hydroxymethylfurfural. *Chem. Soc. Rev.* **2020**, *49*, 4273–4306. [[CrossRef](#)]
6. Timofeev, K.L.; Kharlamova, T.S.; Ezhov, D.M.; Salaev, M.A.; Svetlichnyi, V.A.; Vodyankina, O.V. Hydroxymethylfurfural oxidation over unsupported Pd-Au alloy catalysts prepared by pulsed laser ablation: Synergistic and compositional effects. *Appl. Catal. A Gen.* **2023**, *656*, 119121. [[CrossRef](#)]
7. Bai, Y.; Dou, Y.; Xie, L.-H.; Rutledge, W.; Li, J.-R.; Zhou, H.-C. Zr-based metal–organic frameworks: Design, synthesis, structure, and applications. *Chem. Soc. Rev.* **2016**, *45*, 2327–2367. [[CrossRef](#)]
8. Hall, J.N.; Bollini, P. Structure, characterization, and catalytic properties of open-metal sites in metal organic frameworks. *React. Chem. Eng.* **2019**, *4*, 207–222. [[CrossRef](#)]
9. Ding, Q.; Liu, Y.; Shi, C.; Xiao, J.; Dai, W.; Liu, D.; Chen, H.; Li, B.; Liu, J. Applications of ROS-Induced Zr-MOFs Platform in Multimodal Synergistic Therapy. *Mini Rev. Med. Chem.* **2021**, *21*, 1718–1733. [[CrossRef](#)]
10. Chen, J.; Liu, R.; Guo, Y.; Chen, L.; Gao, H. Selective Hydrogenation of Biomass-Based 5-Hydroxymethylfurfural over Catalyst of Palladium Immobilized on Amine-Functionalized Metal–Organic Frameworks. *ACS Catal.* **2014**, *5*, 722–733. [[CrossRef](#)]
11. Zhang, F.; Zheng, S.; Xiao, Q.; Zhong, Y.; Zhu, W.; Lin, A.; El-Shall, M.S. Synergetic catalysis of palladium nanoparticles encaged within amine-functionalized UiO-66 in the hydrodeoxygenation of vanillin in water. *Green Chem.* **2016**, *18*, 2900–2908. [[CrossRef](#)]
12. Kollmannsberger, K.L.; Kronthaler, L.; Jinschek, J.R.; Fischer, R.A. Defined metal atom aggregates precisely incorporated into metal–organic frameworks. *Chem. Soc. Rev.* **2022**, *51*, 9933–9959. [[CrossRef](#)]
13. Xu, Z.; Wu, Z.; Huang, S.; Ye, K.; Jiang, Y.; Liu, J.; Liu, J.; Lu, X.; Li, B. A metal-organic framework-based immunomodulatory nanopatform for anti-atherosclerosis treatment. *J. Control. Release* **2023**, *354*, 615–625. [[CrossRef](#)]
14. Ding, Q.; Xu, Z.; Zhou, L.; Rao, C.; Li, W.; Muddassir, M.; Sakiyama, H.; Li, B.; Ouyang, Q.; Liu, J. A multimodal Metal–Organic framework based on unsaturated metal site for enhancing antitumor cytotoxicity through Chemo-Photodynamic therapy. *J. Colloid Interface Sci.* **2022**, *621*, 180–194. [[CrossRef](#)]
15. Wang, G.; He, C.-T.; Huang, R.; Mao, J.; Wang, D.; Li, Y. Photoinduction of Cu Single Atoms Decorated on UiO-66-NH<sub>2</sub> for Enhanced Photocatalytic Reduction of CO<sub>2</sub> to Liquid Fuels. *J. Am. Chem. Soc.* **2020**, *142*, 19339–19345. [[CrossRef](#)]

16. Wang, J.; Hu, Y.; Chen, G.; Dong, Y. Cu(II)/Cu(0)/UiO-66-NH<sub>2</sub>: Base metal@MOFs as heterogeneous catalysts for olefin oxidation and reduction. *Chem. Commun.* **2016**, *52*, 13116–13119. [[CrossRef](#)]
17. Luan, Y.; Qi, Y.; Gao, H.; Zheng, N.; Wang, G. Synthesis of an amino-functionalized metal–organic framework at a nanoscale level for gold nanoparticle deposition and catalysis. *J. Mater. Chem. A* **2014**, *2*, 20588–20596. [[CrossRef](#)]
18. Isaeva, V.I.; Chernyshev, V.V.; Vergun, V.V.; Arkhipov, D.A.; Deyko, G.S.; Glukhov, L.M.; Kapustin, G.I.; Tkachenko, O.P.; Kustov, L.M. The Impact of Functionality and Porous System of Nanostructured Carriers Based on Metal–Organic Frameworks of UiO-66-Type on Catalytic Performance of Embedded Au Nanoparticles in Hydroamination Reaction. *Catalysts* **2023**, *13*, 133. [[CrossRef](#)]
19. Bajpai, V.K.; Haldorai, Y.; Khan, I.; Sonwal, S.; Singh, M.P.; Yadav, S.; Paray, B.A.; Jan, B.L.; Kang, S.-M.; Huh, Y.S.; et al. Au@Zr-based metal–organic framework composite as an immunosensing platform for determination of hepatitis B virus surface antigen. *Microchim. Acta* **2021**, *188*, 365. [[CrossRef](#)]
20. Yin, D.; Li, C.; Ren, H.; Liu, J.; Liang, C. Gold-Palladium-Alloy-Catalyst Loaded UiO-66-NH<sub>2</sub> for Reductive Amination with Nitroarenes Exhibiting High Selectivity. *ChemistrySelect* **2018**, *3*, 5092–5097. [[CrossRef](#)]
21. Subudhi, S.; Mansingh, S.; Tripathy, S.P.; Mohanty, A.; Mohapatra, P.; Rath, D.; Parida, K. The fabrication of Au/Pd plasmonic alloys on UiO66-NH<sub>2</sub>: An efficient visible light-induced photocatalyst towards the Suzuki Miyaura coupling reaction under ambient conditions. *Catal. Sci. Technol.* **2019**, *9*, 6585–6597. [[CrossRef](#)]
22. Liu, J.; Jiang, S.; Zhang, Q. Doping copper ions in a metal-organic framework (UiO-66-NH<sub>2</sub>): Location effect examined by ultrafast spectroscopy. *Chin. J. Chem. Phys.* **2020**, *33*, 394–400. [[CrossRef](#)]
23. Xiao, J.-D.; Shang, Q.; Xiong, Y.; Zhang, Q.; Luo, Y.; Yu, S.-H.; Jiang, H.-L. Boosting Photocatalytic Hydrogen Production of a Metal–Organic Framework Decorated with Platinum Nanoparticles: The Platinum Location Matters. *Angew. Chem. Int. Ed.* **2016**, *55*, 9389–9393. [[CrossRef](#)] [[PubMed](#)]
24. Chavan, S.M.; Shearer, G.C.; Svelle, S.; Olsbye, U.; Bonino, F.; Ethiraj, J.; Lillerud, K.P.; Bordiga, S. Synthesis and Characterization of Amine-Functionalized Mixed-Ligand Metal–Organic Frameworks of UiO-66 Topology. *Inorg. Chem.* **2014**, *53*, 9509–9515. [[CrossRef](#)] [[PubMed](#)]
25. Aghajanzadeh, M.; Zamani, M.; Molavi, H.; Manjili, H.K.; Danafar, H.; Shojaei, A. Preparation of Metal–Organic Frameworks UiO-66 for Adsorptive Removal of Methotrexate from Aqueous Solution. *J. Inorg. Organomet. Polym. Mater.* **2018**, *28*, 177–186. [[CrossRef](#)]
26. Kandiah, M.; Nilsen, M.H.; Usseglio, S.; Jakobsen, S.; Olsbye, U.; Tilsted, M.; Larabi, C.; Quadrelli, E.A.; Bonino, F.; Lillerud, K.P. Synthesis and Stability of Tagged UiO-66 Zr-MOFs. *Chem. Mater.* **2010**, *22*, 6632–6640. [[CrossRef](#)]
27. Hadjiivanov, K.I.; Panayotov, D.A.; Mihaylov, M.Y.; Ivanova, E.Z.; Chakarova, K.K.; Andonova, S.M.; Drenchev, N.L. Power of Infrared and Raman Spectroscopies to Characterize Metal-Organic Frameworks and Investigate Their Interaction with Guest Molecules. *Chem. Rev.* **2021**, *121*, 1286–1424. [[CrossRef](#)]
28. Lee, T.; Chang, Y.H.; Lee, H.L. Crystallization process development of metal–organic frameworks by linking secondary building units, lattice nucleation and luminescence: Insight into reproducibility. *CrystEngComm* **2017**, *19*, 426–441. [[CrossRef](#)]
29. Shastri, A.; Das, A.K.; Krishnakumar, S.; Singh, P.J.; Sekhar, B.N.R. Spectroscopy of N,N-dimethylformamide in the VUV and IR regions: Experimental and computational studies. *J. Chem. Phys.* **2017**, *147*, 224305. [[CrossRef](#)]
30. Chavan, S.; Vitillo, J.G.; Gianolio, D.; Zavorotynska, O.; Civalleri, B.; Jakobsen, S.; Nilsen, M.H.; Valenzano, L.; Lamberti, C.; Lillerud, K.P.; et al. H<sub>2</sub> storage in isostructural UiO-67 and UiO-66 MOFs. *Phys. Chem. Chem. Phys.* **2012**, *14*, 1614–1626. [[CrossRef](#)]
31. Sun, D.; Liu, W.; Qiu, M.; Zhang, Y.; Li, Z. Introduction of a mediator for enhancing photocatalytic performance via post-synthetic metal exchange in metal–organic frameworks (MOFs). *Chem. Commun.* **2015**, *51*, 2056–2059. [[CrossRef](#)]
32. Thommes, M.; Kaneko, K.; Neimark, A.; Olivier, J.; Rodriguez-Reinoso, F.; Rouquerol, J.; Sing, K. Physisorption of gases, with special reference to the evaluation of surface area and pore size distribution (IUPAC Technical Report). *Pure Appl. Chem.* **2015**, *87*, 1051–1069. [[CrossRef](#)]
33. Han, Y.; Liu, M.; Li, K.; Zuo, Y.; Wei, Y.; Xu, S.; Zhang, G.; Song, C.; Zhang, Z.; Guo, X. Facile synthesis of morphology and size-controlled zirconium metal–organic framework UiO-66: The role of hydrofluoric acid in crystallization. *CrystEngComm* **2015**, *17*, 6434–6440. [[CrossRef](#)]
34. Ten, S.; Torbina, V.V.; Zaikovskii, V.I.; Kulinich, S.A.; Vodyankina, O.V. Bimetallic AgPd/UiO-66 Hybrid Catalysts for Propylene Glycol Oxidation into Lactic Acid. *Materials* **2020**, *13*, 5471. [[CrossRef](#)]
35. Zhu, G.; Graver, R.; Emdadi, L.; Liu, B.; Choi, K.Y.; Liu, D. Synthesis of zeolite@metal–organic framework core–shell particles as bifunctional catalysts. *RSC Adv.* **2014**, *4*, 30673–30676. [[CrossRef](#)]
36. Friebe, S.; Geppert, B.; Steinbach, F.; Caro, J. Metal–Organic Framework UiO-66 Layer: A Highly Oriented Membrane with Good Selectivity and Hydrogen Permeance. *ACS Appl. Mater. Interfaces* **2017**, *9*, 12878–12885. [[CrossRef](#)]
37. Wu, Y.; Weckhuysen, B.M. Separation and Purification of Hydrocarbons with Porous Materials. *Angew. Chem. Int. Ed.* **2021**, *60*, 18930–18949. [[CrossRef](#)]
38. Guan, T.; Li, X.; Fang, W.; Wu, D. Efficient removal of phosphate from acidified urine using UiO-66 metal-organic frameworks with varying functional groups. *Appl. Surf. Sci.* **2020**, *501*, 144074. [[CrossRef](#)]
39. Ibrahim, A.H.; El-Mehalmey, W.A.; Haikal, R.R.; Safy, M.E.A.; Amin, M.; Shatla, H.R.; Karakalos, S.G.; Alkordi, M.H. Tuning the Chemical Environment within the UiO-66-NH<sub>2</sub> Nanocages for Charge-Dependent Contaminant Uptake and Selectivity. *Inorg. Chem.* **2019**, *58*, 15078–15087. [[CrossRef](#)]

40. Kosmulski, M. *Surface Charging and Points of Zero Charge (Surfactant Science)*; CRC Press: Boca Raton, FL, USA, 2009; p. 1065.
41. Kuwahara, Y.; Kango, H.; Yamashita, H. Catalytic Transfer Hydrogenation of Biomass-Derived Levulinic Acid and Its Esters to  $\gamma$ -Valerolactone over Sulfonic Acid-Functionalized UiO-66. *ACS Sustain. Chem. Eng.* **2016**, *5*, 1141–1152. [[CrossRef](#)]
42. Xu, H.; Chen, M.; Ji, M. Solid Lewis acid-base pair catalysts constructed by regulations on defects of UiO-66 for the catalytic hydrogenation of cinnamaldehyde. *Catal. Today* **2022**, *402*, 52–59. [[CrossRef](#)]
43. Caratelli, C.; Hajek, J.; Cirujano, F.G.; Waroquier, M.; Llabrés i Xamena, F.X.; Van Speybroeck, V. Nature of active sites on UiO-66 and beneficial influence of water in the catalysis of Fischer esterification. *J. Catal.* **2017**, *352*, 401–414. [[CrossRef](#)]
44. Ouellette, R.J.; Rawn, J.D. 23—Amines and Amides. In *Organic Chemistry Study Guide*; Elsevier: Amsterdam, The Netherlands, 2015; pp. 465–494. [[CrossRef](#)]
45. Giambiagi, M.; de Giambiagi, M.S.; Mundim, K.C. Definition of a multicenter bond index. *Struct. Chem.* **1990**, *1*, 423–427. [[CrossRef](#)]
46. Wang, K.; Gu, J.; Yin, N. Efficient Removal of Pb(II) and Cd(II) Using NH<sub>2</sub>-Functionalized Zr-MOFs via Rapid Microwave-Promoted Synthesis. *Ind. Eng. Chem. Res.* **2017**, *56*, 1880–1887. [[CrossRef](#)]
47. Zhang, Y.; Guan, W.; Song, H.; Wei, Y.; Jin, P.; Li, B.; Yan, C.; Pan, J.; Yan, Y. Coupled acid and base UiO-66-type MOFs supported on g-C<sub>3</sub>N<sub>4</sub> as a bi-functional catalyst for one-pot production of 5-HMF from glucose. *Microporous Mesoporous Mater.* **2020**, *305*, 110328. [[CrossRef](#)]
48. Tanabe, K. *Solid Acids and Bases: Their Catalytic Properties*, 1st ed.; Academic Press: Cambridge, MA, USA, 1971; 184p.

**Disclaimer/Publisher's Note:** The statements, opinions and data contained in all publications are solely those of the individual author(s) and contributor(s) and not of MDPI and/or the editor(s). MDPI and/or the editor(s) disclaim responsibility for any injury to people or property resulting from any ideas, methods, instructions or products referred to in the content.